

Early MAVEN Deep Dip campaign reveals thermosphere and ionosphere variability

S. Bouger,^{1*} B. Jakosky,² J. Halekas,³ J. Grebowsky,⁴ J. Luhmann,⁵ P. Mahaffy,⁴ J. Connerney,⁴ F. Eparvier,² R. Ergun,² D. Larson,⁵ J. McFadden,⁵ D. Mitchell,⁵ N. Schneider,² R. Zurek,⁶ C. Mazelle,^{7,8} L. Andersson,² D. Andrews,⁹ D. Baird,¹⁰ D. N. Baker,² J. M. Bell,¹¹ M. Benna,⁴ D. Brain,² M. Chaffin,² P. Chamberlin,⁴ J.-Y. Chaufray,¹² J. Clarke,¹³ G. Collinson,⁴ M. Combi,¹ F. Crary,² T. Cravens,¹⁴ M. Crismani,² S. Curry,⁵ D. Curtis,⁵ J. Deighan,² G. Delory,⁵ R. Dewey,² G. DiBraccio,⁴ C. Dong,¹ Y. Dong,² P. Dunn,⁵ M. Elrod,⁴ S. England,⁵ A. Eriksson,⁹ J. Espley,⁴ S. Evans,¹⁵ X. Fang,² M. Fillingim,⁵ K. Fortier,² C. M. Fowler,² J. Fox,¹⁶ H. Gröller,¹⁷ S. Guzewich,⁴ T. Hara,⁵ Y. Harada,⁵ G. Holsclaw,² S. K. Jain,² R. Jolitz,⁵ F. Leblanc,¹² C. O. Lee,⁵ Y. Lee,¹ F. Lefevre,¹² R. Lillis,⁵ R. Livi,⁵ D. Lo,¹⁷ Y. Ma,¹⁸ M. Mayyasi,¹³ W. McClintock,² T. McElwain,² R. Modolo,¹² F. Montmessin,¹² M. Morooka,² A. Nagy,¹ K. Olsen,¹ W. Peterson,² A. Rahmati,¹⁴ S. Ruhunusiri,³ C. T. Russell,¹⁸ S. Sakai,¹⁴ J.-A. Sauvage,^{7,8} K. Seki,¹⁹ M. Steckiewicz,^{7,8} M. Stevens,²⁰ A. I. F. Stewart,² A. Stiepen,² S. Stone,¹⁷ V. Tenishev,¹ E. Thiemann,² R. Tolson,¹¹ D. Toublanc,^{7,8} M. Vogt,¹³ T. Weber,² P. Withers,¹³ T. Woods,² R. Yelle¹⁷

The Mars Atmosphere and Volatile Evolution (MAVEN) mission, during the second of its Deep Dip campaigns, made comprehensive measurements of martian thermosphere and ionosphere composition, structure, and variability at altitudes down to ~130 kilometers in the subsolar region. This altitude range contains the diffusively separated upper atmosphere just above the well-mixed atmosphere, the layer of peak extreme ultraviolet heating and primary reservoir for atmospheric escape. In situ measurements of the upper atmosphere reveal previously unmeasured populations of neutral and charged particles, the homopause altitude at approximately 130 kilometers, and an unexpected level of variability both on an orbit-to-orbit basis and within individual orbits. These observations help constrain volatile escape processes controlled by thermosphere and ionosphere structure and variability.

The Mars upper atmosphere—the top ~100 to 500 km encompassing the thermosphere, ionosphere, and lower portion of the exosphere—constitutes the reservoir that regulates present-day escape processes from the planet. Understanding the coupling of the lower to upper atmosphere is essential to characterizing energy deposition and upward flow of material that can ultimately result in neutral and ion escape from the planet (1). In principle, it is possible to constrain the short-term (current) atmospheric escape rates making use of the Mars Atmosphere and Volatile Evolution (MAVEN) measurements over this reservoir region and at higher altitudes. However, without knowledge of the physics and chemistry operating in this reservoir region and driving its variations (such as solar cycle, seasonal, and diurnal), it is not possible to reliably extrapolate the results over evolutionary history. The characterization of this upper atmosphere reservoir is therefore one of the major science objectives of the MAVEN mission (2).

Here, we present measurements of subsolar neutral atmospheric composition and temperature, together with ionospheric charged-particle and magnetic-field structure, extending from

near the homopause to above the exobase, as enabled by MAVEN's "Deep Dip" campaigns. During each week-long campaign, periapsis is lowered from a nominal altitude of ~150 to 170 km to ~120 to 135 km in order to reach a peak mass density of ~2 to 3.5 kg/km³. This strategy allows direct in situ sampling of the entire reservoir region for atmospheric escape, from the exosphere downward to near the homopause (3). During each orbit, MAVEN makes in situ measurements along the elliptical orbit track of neutral and thermal ion species, thermal electrons, magnetic fields, and suprathermal electrons and ions, using a suite of science instruments (4). Periapsis migrates around the planet during the course of the mission, providing comprehensive coverage of latitude and local time, and deep dips are dispersed in time in order to sample different regions of interest (5). We focused on the second campaign (DD2), spanning 17 to 22 April 2015, which provided sampling near the subsolar region (local time = 12 to 13), late in the martian year ($L_s \sim 327$ to 330), and near the equator (6). Measurements of the subsolar region are important for constraining neutral-ion chemistry and dynamics in numerical simulations that estimate both neutral and ion escape rates. In addition,

thermosphere-ionosphere structure and neutral temperatures are believed to be controlled in part by the changing solar extreme ultraviolet-ultraviolet (EUV-UV) fluxes; this forcing is greatest at low solar zenith angles (SZAs).

We present two sequential DD2 orbits (O1085 and O1086, on 22 April 2015), the first focusing on charged-particle and field measurements and the second on neutral composition and temperatures (Fig. 1). The thermal ion and neutral measurements were made with NGIMS on alternating orbits, necessitating the emphasis on two sequential orbit passes. Both of these orbits had periapses in a region with moderate crustal magnetic fields and occurred during nominal upstream solar wind conditions. We also examined the full suite of DD2 orbits for orbit-to-orbit neutral density and temperature variability.

Neutral composition and temperature observations

The martian upper atmosphere between the exosphere and the homopause encompasses the region of changing importance of heterogeneous (diffusive separation) and homogeneous (small-scale mixing) processes that control the density structure, the location of the peak solar EUV energy deposition, and the main reservoir for escaping particles (1). During nominal orbits, MAVEN does not reach the well-mixed atmosphere, but during the Deep Dip campaigns, MAVEN instruments can sample the column extending from near the homopause upward into the exosphere, where neutral and ion escape can occur.

During the DD2 campaign, MAVEN successfully made measurements of the structure and variability of this critical altitude range in the subsolar region. Previously, the thermospheric neutral composition had only been directly measured in situ with the Upper Atmosphere Mass Spectrometer (UAMS) instruments onboard the descending Viking Landers 1 and 2 (7). These two descent profiles provided measurements for

¹CLASP Department, University of Michigan, Ann Arbor, MI, USA. ²Laboratory for Atmospheric and Space Physics, University of Colorado, Boulder, CO, USA. ³Department of Physics and Astronomy, University of Iowa, Iowa City, IA, USA. ⁴NASA/Goddard Space Flight Center, Greenbelt, MD, USA. ⁵Space Sciences Laboratory, University of California at Berkeley, Berkeley, CA, USA. ⁶Jet Propulsion Laboratory, California Institute of Technology, Pasadena, CA, USA.

⁷CNRS/Institut de Recherche en Astrophysique et Planétologie, Toulouse, France. ⁸University Paul Sabatier, Toulouse, France. ⁹Swedish Institute of Space Physics, Kiruna, Sweden. ¹⁰NASA/Johnson Space Center, Houston, TX, USA. ¹¹National Institute of Aerospace, Hampton, VA, USA. ¹²Laboratoire Atmosphères, Milieux, Observations Spatiales /CNRS, Verrières-le-Buisson, France. ¹³Department of Astronomy, Boston University, Boston, MA, USA.

¹⁴Department of Physics and Astronomy, University of Kansas, Lawrence, KS, USA. ¹⁵Computational Physics, Springfield, VA, USA. ¹⁶Department of Physics, Wright State University, Fairborn, OH, USA. ¹⁷Lunar and Planetary Laboratory, University of Arizona, Tucson, AZ, USA.

¹⁸Institute of Geophysics and Planetary Physics, University of California, Los Angeles, Los Angeles, CA, USA. ¹⁹Solar-Terrestrial Environment Laboratory, Nagoya University, Nagoya, Aichi, Japan. ²⁰Naval Research Laboratory, Washington, DC, USA.

*Corresponding author. E-mail: bouger@umich.edu

SZA near 44° at low-to-middle latitude for two afternoon locations during solar minimum and near aphelion conditions. The total mass density of the Mars thermosphere has also been measured by several spacecraft accelerometers (5, 8, 9).

The MAVEN NGIMS instrument measures the neutral composition of the major gas species (such as He, N, O, CO, N₂, O₂, NO, Ar, and CO₂) and their major isotopes, with a vertical resolution of ~5 km for targeted species and a target accuracy of <25% for most of these species (10). Corresponding temperatures can be derived from the neutral-scale heights. These multispecies measurements are obtained along an orbit trajectory that combines both vertical and horizontal variations of the upper atmosphere structure (1). These convolved variations cannot be separated without the use of numerical models.

Four key neutral species are presented (CO₂, Ar, N₂, and O) for the inbound leg (Fig. 2). The NGIMS and Mars Global Ionosphere-Thermosphere Model (M-GITM)-simulated CO₂, N₂, and Ar density profiles match reasonably well throughout the altitude range (supplementary text S1) (9). For example, in the range of 160 to 220 km, M-GITM diurnal variations of CO₂ encompass NGIMS densities quite well, whereas below 160 km, M-GITM underestimates NGIMS CO₂ densities (up to a factor of ~2 at 130 km). Both models and observations show an exponential variation of density with altitude. The scale heights of these species are different at higher altitudes, with most of them (CO₂, Ar, and N₂) showing a common scale height as 130 km is approached. This is consistent with a homopause near 130 km, but quantitative confirmation of the precise homopause altitude cannot be seen in this figure. Atomic O scale heights do not follow this pattern of transitioning scale heights because local chemical production and loss processes are important (3). These multispecies, subsolar, neutral-atmosphere measurements capture near-homopause (~130 km) to exosphere (above ~200 km) structure together on the same orbit.

The atomic O density profiles from NGIMS (Fig. 2) constrain the ion-neutral chemistry, thermal heat budget, and dynamics of the Mars dayside upper atmosphere (1). NGIMS-measured O densities have been corrected for (i) open-source neutral beaming (OSNB) retrieval, (ii) contributions from CO₂ at lower altitudes, and (iii) “pile up” RAM direction enhancement of densities when approaching periapsis altitudes, with largest corrections present for the higher densities during Deep Dip orbits. Atomic O densities are determined to be reliable (within the ~25% error) down to ~150 km. Comparison of measured and simulated DD2 atomic O profiles shows reasonable agreement at all altitudes, with densities at ~200 km close to $\sim 5.0 \times 10^7$ to 6.0×10^7 cm⁻³. These NGIMS-measured O densities are nearly a factor of ~5 larger than corresponding Mars Express (MEx)/Spectroscopy for Investigation of Characteristics of the Atmosphere of Mars (SPICAM) estimates derived via remote sensing (11). The differences in the seasonal (equinox versus aphelion) and solar cycle (solar moderate versus minimum)

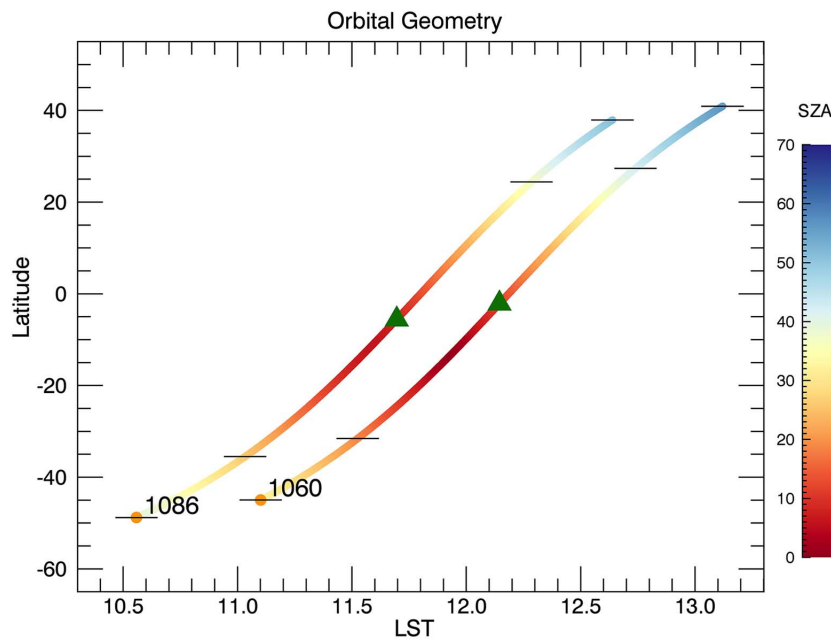


Fig. 1. MAVEN Deep Dip 2 orbital geometry. MAVEN spacecraft “along-track” latitude versus local time coverage of DD2 sampling below 500 km is illustrated (NGIMS measurements are limited to this altitude range). Beginning (O1060) and ending (O1086) orbit information is provided, capturing both inbound and outbound legs, plus the periapsis location (triangles). The 500 and 300 km points on each leg are also delineated by black tick marks. The start of each inbound leg is identified (yellow dots). Specific orbits selected for detailed investigation (O1085 and O1086) fall in between these bounding orbits. SZA is also indicated along these orbit trajectories.

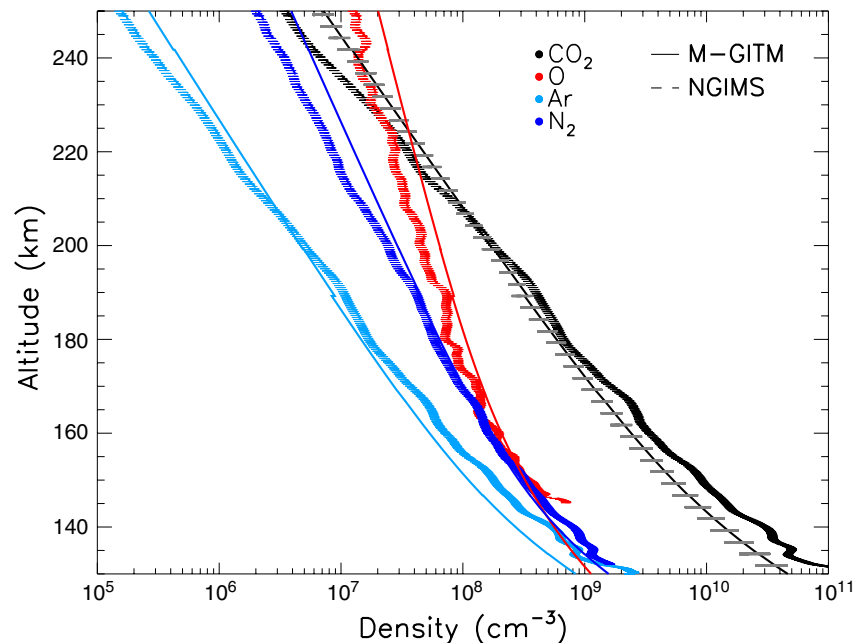


Fig. 2. Neutral density environment near periapsis during the subsolar DD2 campaign. These altitude profiles are provided over ~130 to 250 km specifically for a single orbit (O1086) from 22 April 2015 (supplementary text S2). Four key neutral species are plotted (CO₂, Ar, N₂, and O) for the inbound leg (hashed curves). Simulated subsolar density profiles from the M-GITM, calculated at the location of the spacecraft along its orbit for the solar moderate case (Equinox), are overplotted (solid curves) for comparison (supplementary text S1). The plotted NGIMS densities have been processed by using a 20-s polynomial time-averaging technique so as to remove high-frequency, small-scale variations (supplementary text S3). Calculated NGIMS error bars are included in each profile (supplementary text S4). In addition, 1-[g] variance bars are added to the 1-SOL averaged M-GITM CO₂ densities in order to illustrate their expected diurnal variation.

sampling between these two data sets may be responsible for this factor of ~ 5 variation. This substantial variation in atomic O densities at 200 km may have important implications for mass loading of the solar wind because thermospheric and exospheric O densities are simulated to respond similarly to solar cycle and seasonal changes (12).

The O/CO₂ ratio is expected to vary with the changing solar EUV-UV fluxes reaching Mars (affecting CO₂ photolysis rates) and the ability of the thermospheric circulation to transport atomic O around the planet (1). A data-model comparison shows that the altitude at which this ratio is unity occurs around ~ 225 km for both NGIMS and M-GITM profiles near the subsolar region (Fig. 3A). This profile determines that the O abundance becomes important above 225 km in the Mars exosphere. This cold O constraint is important for making proper calculations of hot O escape (1). Similarly, this O/CO₂ ratio near 150 km (about ~ 20 km above the expected primary ion peak) is measured to be $\sim 4.0\%$ and is consistent with the NGIMS-measured O₂⁺/CO₂⁺ ratio of ~ 6.0 at the same altitude. This occurs because this ion ratio is directly controlled by the atomic O abundance (13).

As the measured N₂ and CO₂ profiles approach ~ 130 km, the N₂/CO₂ ratio converges on the bulk atmosphere value of $\sim 2.0\%$ (Fig. 3B), recently measured by the Mars Science Laboratory (MSL) Sample Analysis at Mars Suite (SAMS) instrument (14). The decrease of the ratio with decreasing height is expected because the N₂ scale height is larger than that for CO₂. The convergence of this NGIMS N₂/CO₂ ratio to the constant value of $\sim 2.0\%$ near 130 km indicates that the N₂ homopause altitude during this orbit is located at ~ 130 km. In fact, all species are subject to the same small-scale mixing, but each has a slightly different homopause altitude owing to small variations in molecular diffusion coefficients (3). By this same method, the simulated M-GITM N₂/CO₂ ratio places the N₂ homopause at ~ 120 km altitude. The difference between these two homopause altitudes implies that some refinement of the small-scale mixing (eddy diffusion) is needed in the M-GITM code (supplementary text S1) (9). This model adjustment is expected because the homopause altitude is very sensitive to small-scale mixing, which is itself poorly constrained other than by these new MAVEN measurements. In addition, M-GITM assumes the Viking mixed-atmosphere value of the N₂/CO₂ ratio ($\sim 2.7\%$) (7), which is larger than measured by SAMS (14). These NGIMS density profiles provide an important initial determination of the dayside homopause altitude, which was previously estimated from Viking modeling studies to be located between ~ 120 and 130 km (7).

Derived NGIMS and simulated M-GITM average temperature profiles (over the entire DD2 campaign) each include averaging over longitude and various wave features (Fig. 4). These averaged NGIMS temperature profiles are constructed by using the Snowden method with hydrostatic integration over the DD2 averaged Ar and N₂ density profiles (15). Such averaging serves to

smooth out much of the wave structure and determines that the upper-boundary temperature gradients should be close to zero (isothermal).

For M-GITM, simulated temperatures are extracted along each orbit trajectory and subsequently averaged together over all DD2 orbits. The

Fig. 3. Altitude plots

illustrating key neutral density ratios below 300 km for DD2.

These ratios (Top) O/CO₂ and (Bottom) N₂/CO₂ are composed of the same O1086 NGIMS and M-GITM density profiles illustrated in Fig. 2. The O/CO₂ = 1 crossover point near ~ 225 km (for both NGIMS and M-GITM) is indicated with a vertical dashed line. The measured N₂/CO₂ MSL mixed-atmosphere value of $\sim 2.0\%$ is also indicated with a vertical dashed line (14).

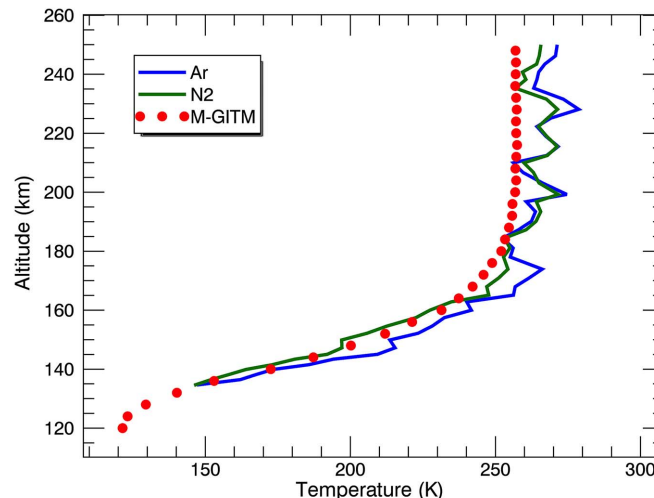
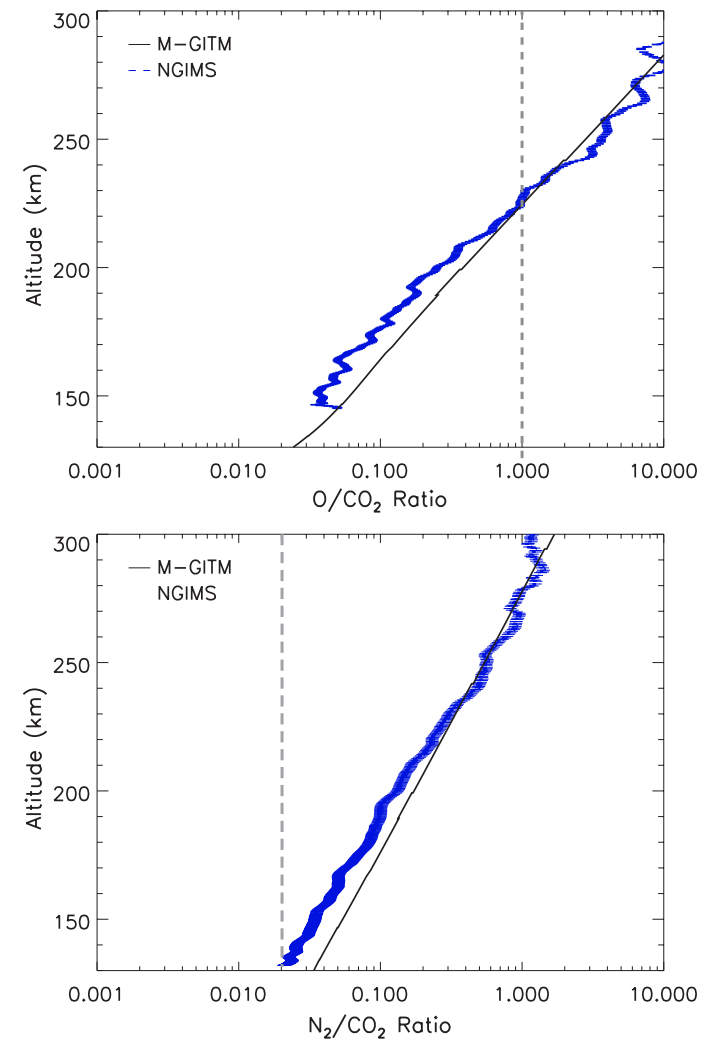


Fig. 4. Profiles of averaged temperature profiles from the entire DD2 campaign. Both NGIMS derived (N₂ and Ar) and M-GITM-simulated temperature profiles are plotted up to 250 km. Mean exospheric temperatures (200 to 250 km) approach ~ 268 K (NGIMS) and ~ 257 K (M-GITM).

observed large vertical temperature gradient over ~140 to 170 km coincides with the peak layer of EUV heating, whereas the topside temperatures approach isothermal values above ~200 km. In particular, exospheric temperatures (T_{exo}) are separately extracted from Ar densities by averaging temperatures over ~200 to 250 km for each orbit, then averaging all orbit values together. CO₂ and N₂ densities could also be used, yielding similar temperatures (16). The resulting NGIMS extracted mean T_{exo} value of ~268 K is compared with the simulated mean value of ~257 K from M-GITM.

This MAVEN dayside temperature profile is the result of averaging over several DD2 orbits and consequently masks the significant orbit-to-orbit (1σ) variability of NGIMS exospheric temperatures (268 ± 19 K) (16). This temporal behavior is similar to that observed from MEx dayside measurements ($\sim 270 \pm 25$ K) extracted from SPICAM dayglow scale heights over 2004–2009 (17, 18). Furthermore, M-GITM simulations (primarily solar-driven) cannot capture this orbit-to-orbit variability, yet M-GITM simulations can reasonably match the DD2 orbit mean T_{exo} value. This large orbit-to-orbit variability implies that dayside thermospheric temperatures are not controlled exclusively by solar EUV forcing, as models might predict (17, 18).

Repeated MAVEN sampling at the 200-km level provides another method for characterization of upper-atmosphere variability near the base of the exosphere. NGIMS neutral densities show a substantial orbit-to-orbit variability throughout the DD2 campaign. Altitude profiles of O and CO₂ densities spanning 14 orbits from O1060 to O1086 show substantial variability on ~4- to 5-hour time scales (Fig. 5). The altitude at which the O/CO₂ ratio crosses through unity varies from ~225 to 238 km for these orbits. The O and CO₂ variations at a constant altitude are also substantial, with measured O densities at 200 km ranging from $\sim 5.0 \times 10^7$ to $\sim 1.0 \times 10^8 \text{ cm}^{-3}$ (factor of 2), whereas CO₂ densities vary from $\sim 1.3 \times 10^8$ to $\sim 3.5 \times 10^8 \text{ cm}^{-3}$ (factor of 2.7). These density variations are notable, especially when combined with exospheric temperature variations described above. The implication is that upper-atmosphere structure near 200 km varies substantially from orbit to orbit (on at least ~5-hour time scales), and also as a function of season and solar cycle as illustrated by MEx versus MAVEN results. Orbit-to-orbit variability may be driven from below owing to gravity wave interactions with the global wind structure and small-scale mixing processes (19, 20). This combined density and temperature variability at this exobase altitude (21) ultimately has a direct impact upon volatile escape rates (1).

Charged-particle and magnetic-field observations

Plasma measurements extending from the magnetosphere down to the main peak of the sub-solar martian ionosphere have been collected by MAVEN. MGS and MEx previously explored the induced magnetosphere and the transition to the upper ionosphere (22, 23), but neither mission carried a complete complement of plasma instru-

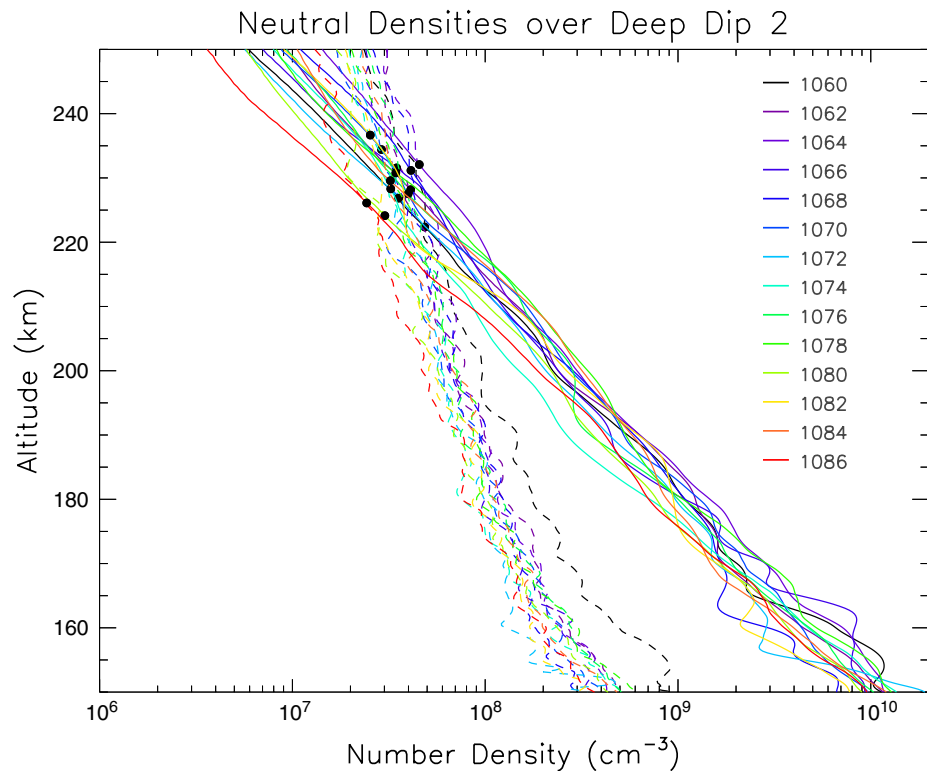


Fig. 5. Altitude plots of O and CO₂ densities over 150 to 250 km. NGIMS O (dashed lines) and CO₂ (solid lines) density profiles are plotted throughout the DD2 campaign, spanning 14 orbits from O1060 to O1086. Separate profiles are color-coded for orbit identification. The black dots for each orbit correspond to the crossing point at which the O/CO₂ ratio is unity. These altitudes range from ~225 to 238 km. The mean height is 230.5 ± 2.5 km.

mentation. Meanwhile, characterization of the lower-altitude collisional ionosphere has primarily used remote sounding techniques (24, 25), revealing variable structure (26) and only occasionally a Venus-like ionopause (27). Viking provided the only previous direct measurements of lower ionospheric structure and composition (13), but only in a narrow range of SZA.

Measurements from MAG (28), SWEA (2), SWIA (29), LPW (30), and NGIMS (10) reveal the complex morphology of the inner magnetosphere and ionosphere (Figs. 6 and 7). Periapsis for this orbit (O1085) occurred at 48°W, 6°S, in a region with moderate crustal magnetic fields, at an altitude of ~130 km and SZA of ~5°. During this period, the spacecraft remained below the induced magnetospheric boundary until 02:18 UTC, after which MAVEN observed suprathermal particles characteristic of the magnetosheath. Before 02:18 UTC, electron spectra displayed features characteristic of atmospheric photoelectrons throughout. Outside of the main peak of the ionosphere (before 02:02 and after 02:12 UTC), in the transport-dominated regime (above ~200 km, major ion lifetimes are ~ 600 s), charged-particle populations and magnetic fields show substantial structure, likely consisting of a mix of transient variations and horizontal and/or vertical structure. O⁺ and O₂⁺ dominate the thermal ion composition, with both varying over orders of magnitude, particularly on the outbound pass. The draped magnetic-field rotations, compositional changes,

and electron temperature changes associated with the ion density layers at L3 and L4 and the intervening density depletions suggest that these represent primarily temporal variations, implying rapid ionospheric reconfigurations, indicative of substantial transport and/or strong compressional waves.

At times L1 and L2, the spacecraft passed sharp thermal ion density layers (more pronounced on the inbound segment). At the same locations, MAVEN observed the signatures of localized currents, visible as a discontinuity in the magnetic field [and a rotation toward a more horizontal field below the layers (Fig. 7)]. These features occurred just above a transition to a smoothly varying photoelectron population, which is consistent with the collisional photochemically controlled region of the ionosphere (31). This ion layer may represent the topside layer previously seen in radar (32) and radio sounding (33) by MEx [perhaps also in the Viking-2 descent (13)] but appears narrower (~5 to 10 km) than is apparent from remote measurements. The sharpness of the layer in comparison with expected variations in neutral density and EUV energy deposition implies vertical transport and suggests that it could represent a transition between a region dominated by draped and/or induced magnetic fields and one dominated by crustal fields (33, 34). Localized electric fields could also play a role, as previously observed at Earth (35). The sharp drop in electron temperature

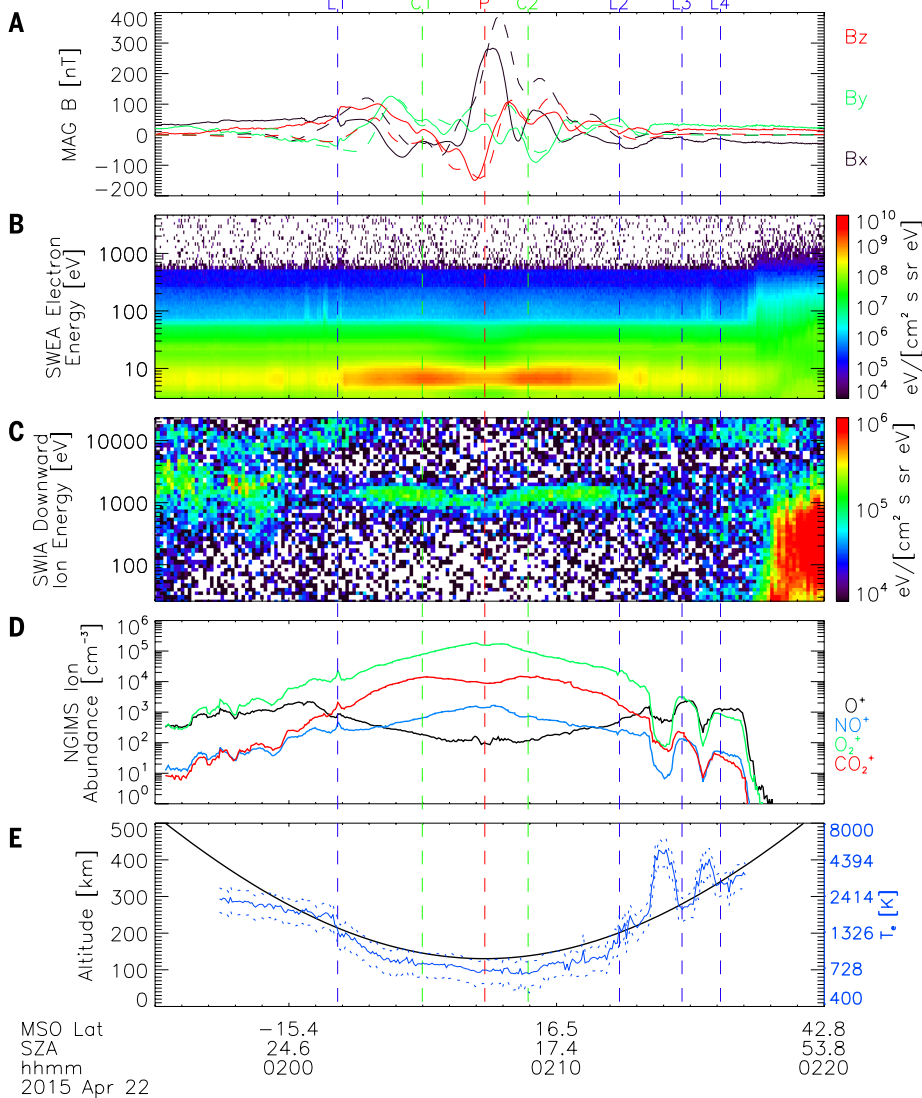


Fig. 6. Plasma environment near periapsis during the subsolar DD2 campaign. These time series plots are provided over 130 to 500 km in a region with moderate crustal fields, during a time period with quiet solar wind conditions, and specifically for O1085 (22 April 2015). (A) MAG-measured (solid) and spherical harmonic model (dashed) crustal magnetic-field vector components (B_x , B_y , and B_z) in Mars-Solar-Orbital coordinates. (B) SWEA energy spectra of suprathermal electrons. (C) SWIA energy spectra of downward-going suprathermal ions. (D) NGIMS abundances of major ion species (O^+ , O_2^+ , CO_2^+ , and NO^+). (E) Spacecraft altitude plus LPW electron temperatures (dashed lines indicate upper and lower bounds, with the solid lines showing the best-fit value). Mars-Solar-Orbital latitude (MSO Lat), solar zenith angle (SZA), and universal time coordinated hour and minute (hhmm) are also provided along the time series below 500 km. Labeled vertical dashed lines are provided to highlight features discussed in the text, including localized ion layers (L1 to L4), peaks in CO_2^+ density (C1 and C2), and periapsis (P), which occurs at 02:07 UTC, at a SZA of ~5°.

below this layer also indicates a topological boundary that locally affects photoelectron transport and suggests that photochemical processes play a role (36).

At lower altitudes, O^+ densities drop rapidly owing to reactions with neutral molecules, but suprathermal photoelectrons and thermal CO_2^+ ions continue to increase in density (with very similar altitude dependence, commensurate with their production primarily from neutral CO_2). These populations peak at the times marked C1 and C2—at altitudes of ~140 km, below which

they decrease—presumably because of recombination and reactions with neutral species. CO_2^+ densities peak at a higher altitude than that of O_2^+ densities, and higher than observed at higher SZA by Viking (13). Meanwhile, O_2^+ densities continue to increase until just above periapsis (time P). The slight decrease in density at periapsis may indicate that the spacecraft reached the main M2 peak of the ionosphere, which is consistent with the periapsis altitude.

The different altitude profiles for major ion species and photoelectrons reflect the variations

in source and loss processes as a function of altitude, stemming from the varying deposition of EUV and other energy inputs (comprehensively measured by MAVEN), changes in neutral composition, and the steeply increasing neutral density. Multifluid magnetohydrodynamic (MHD) model results capture some, but not all, of the observed variations in ion abundance along the orbit track (supplementary text S5) (37, 38). The model correctly reproduces the structure of the dominant O_2^+ ions at altitudes below ~220 km and also captures the structure of the CO_2^+ ions over most of this altitude range. Above ~220 km, in the transport-dominated region, the time-stationary model results cannot adequately capture the transient dynamics. The model also underestimates O^+ density everywhere except periapsis and does not capture the turnover in the CO_2^+ density at low altitudes.

All the major ion species show substantial wave structure on the outbound segment (but not on the inbound), extending almost down to periapsis. This wave structure correlates closely (although not one-to-one everywhere) with fluctuations seen in the neutral density at the same time, suggesting that many of the observed neutral and ion fluctuations might have a common origin, presumably gravity waves (19, 20).

Suprathermal ion measurements provide another probe of collisional processes in the atmosphere. A downward-going population of ~1 keV ions appears between L1 and L2. These ions represent the products of hydrogen energetic neutral atoms (ENAs) produced through charge exchange between solar wind protons and exospheric atoms in the distant corona outside of the bow shock (39, 40). In neutral form, these particles pass through the magnetosphere unaffected by electromagnetic form, maintaining the same velocity as that of the solar wind. Upon encountering the atmosphere, some of the ENAs undergo charge-stripping reactions and regain their charge, allowing MAVEN to measure them. As the neutral density rises, these particles lose energy through numerous collisions with atmospheric gases. The ratio of electron-stripping to charge-exchange cross sections decreases sharply at lower energies, leading to a decrease in the charged fraction of the precipitating hydrogen between C1 and C2. These penetrating solar wind particles represent an additional source of energy to the upper atmosphere, with a different deposition profile from that of EUV. They also provide a proxy measurement of the solar wind, allowing us to infer an upstream solar wind speed of ~500 km/s and density of ~1 cm⁻³ (40).

At higher energies of ~10 to 20 keV, SWIA observes an additional population of precipitating ions, which penetrate well into the photochemical region of the atmosphere (below the “exobase”). When this population extends to higher altitudes, at which suprathermal ion composition measurements in this energy range from STATIC (2) are available, they indicate predominantly O^+ , which is consistent with pickup ions produced by photoionization and charge-transfer reactions in the upstream corona. These precipitating ions

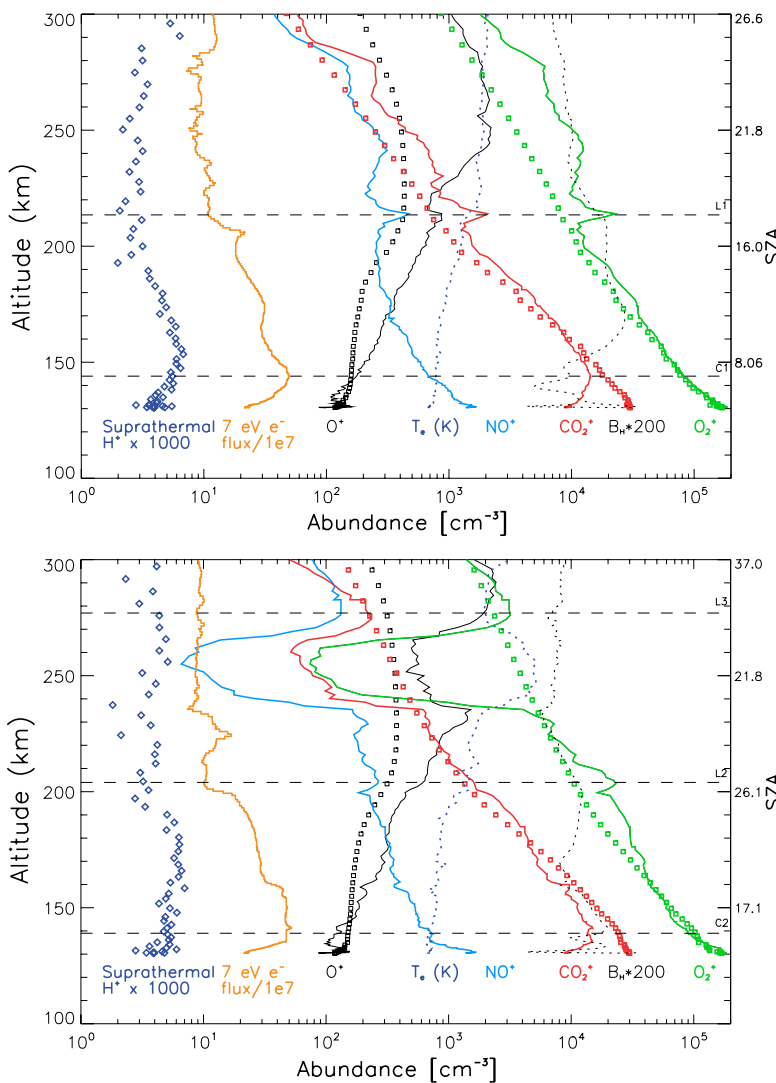


Fig. 7. Altitude plots of ion densities and other plasma fields over 130 to 300 km. NGIMS ion densities are plotted for DD2 orbit O1085, with the corresponding SZA indicated on the right. Four NGIMS key ion species are provided (O^+ , O_2^+ , CO_2^+ , and NO^+) for the (Top) inbound and (Bottom) outbound legs (solid, color-coded curves). Corresponding simulated ion density profiles along the orbit from the multifluid MHD model are plotted (colored squares) for comparison (O^+ , O_2^+ , CO_2^+ only) (supplementary text S5) (37, 38, 42). The measured inbound ratio (O_2^+ / CO_2^+) at 150 km is a factor of ~6, whereas that at 220 km is a factor of ~10. These ratios can be compared with corresponding values of 6 and 7 to 9 from Viking Landers 1 and 2, respectively (13). Also shown for context are scaled values corresponding to the electron temperature, the horizontal magnetic-field magnitude measured by MAG, the suprathermal electron flux measured at 7 eV (the peak of the suprathermal electron flux) by SWEA, and the suprathermal H^+ density measured by SWIA.

may drive sputtering escape of the neutral atmospheric particles (41).

Interpretations and implications

The thermospheric neutral densities and temperatures vary substantially from orbit to orbit, driven in part by tidal and gravity wave forcing. Solar EUV regulation of mean exospheric temperatures (averaged over several orbits) is confirmed for these DD2 measurements, in comparison with solar-driven numerical model simulations. However, this solar forcing does not appear to control interorbital variations of these temperatures. Like the neutral atmosphere to which it is coupled, the ionosphere

revealed by MAVEN is highly dynamic, with substantial structure and temporal variations often observed within a single orbit. Crustal fields clearly affect the structure of the ionosphere, and their effects on transport may lead to the formation of the observed narrow current-carrying plasma layers.

REFERENCES AND NOTES

- S. W. Bougher, T. E. Cravens, J. Grebowsky, J. Luhmann, The aeronomy of Mars: Characterization by MAVEN of the upper atmosphere reservoir that regulates volatile escape. *Space Sci. Rev.* (2014). doi: [10.1007/s11214-014-0053-7](https://doi.org/10.1007/s11214-014-0053-7)
- B. M. Jakosky et al., The Mars Atmosphere and Volatile Evolution (MAVEN) Mission to Mars. *Space Sci. Rev.* (2015). doi: [10.1007/s11214-015-0139-x](https://doi.org/10.1007/s11214-015-0139-x)
- The homopause altitude of a given planetary upper atmosphere is commonly estimated as the altitude at which a given species diffusion coefficient matches the specified eddy diffusion coefficient. This altitude represents that level in the atmosphere below which this species is well mixed (homosphere) and above which molecular diffusion serves to separate species according to their individual scale heights (heterosphere). Each species has its particular homopause altitude, owing to the slight variation of molecular diffusion coefficients by species. In reality, the homopause is not a single altitude level, but a transition region across which these molecular and eddy diffusion processes gradually exchange their dominant roles. For Mars, a common mixed-atmosphere scale height is revealed by CO_2 , Ar , and N_2 below their homopauses. However, photochemically active species (such as O) do not conform to this mixed-atmosphere scale height.
- The MAVEN in situ instruments are the Accelerometer (ACC), Langmuir Probe and Waves (LPW), Magnetometer (MAG), Neutral Gas and Ion Mass Spectrometer (NGIMS), Solar Wind Electron Analyzer (SWEA), Solar Wind Ion Analyzer (SWIA), and Supra-thermal and Thermal Ion Composition (STATIC).
- R. W. Zurek, R. H. Tolson, D. Baird, M. Z. Johnson, S. W. Bougher, M. Z. Johnson, and S. W. Bougher. Application of MAVEN accelerometer and attitude control data to Mars atmospheric characterization. *Space Sci. Rev.* (2014). doi: [10.1007/s11214-014-0095-x](https://doi.org/10.1007/s11214-014-0095-x)
- Areocentric longitude of the Sun, L_s , is used as an angular measure of the Mars year: $L_s = 0, 90, 180$, and 270 correspond to the start of the northern spring, summer, fall, and winter, respectively.
- A. O. Nier, M. B. McElroy, Composition and structure of Mars' upper atmosphere: Results from the neutral mass spectrometers on Viking 1 and 2. *J. Geophys. Res.* **82**, 4341–4349 (1977). doi: [10.1029/JS082i028p04341](https://doi.org/10.1029/JS082i028p04341)
- G. M. Keating et al., The structure of the upper atmosphere of mars: In situ accelerometer measurements from mars global surveyor. *Science* **279**, 1672–1676 (1998). doi: [10.1126/science.279.5357.1672](https://doi.org/10.1126/science.279.5357.1672); pmid: [9497278](https://pubmed.ncbi.nlm.nih.gov/9497278/)
- S. W. Bougher et al., Mars Global Ionosphere-Thermosphere Model: Solar cycle, seasonal and diurnal variations of the Mars upper atmosphere. *J. Geophys. Res.* **120**, 311–342 (2015). doi: [10.1002/2014JE004715](https://doi.org/10.1002/2014JE004715)
- P. R. Mahaffy et al., The Neutral Gas and Ion Mass Spectrometer on the Mars Atmosphere and Volatile Evolution Mission. *Space Sci. Rev.* **185**, 1–25 (2014). doi: [10.1007/s11214-014-0043-9](https://doi.org/10.1007/s11214-014-0043-9)
- J.-Y. Chauffray, F. Leblanc, E. Quemerais, J.-L. Bertaux, Martian oxygen density at the exobase deduced from OI 1304-nm observations by Spectroscopy for the Investigation of the Characteristics of the Atmosphere of Mars on Mars Express. *J. Geophys. Res.* **114** (E2), E02006 (2009). doi: [10.1029/2008JE003130](https://doi.org/10.1029/2008JE003130)
- A. Vaillete, M. R. Combi, S. W. Bougher, V. Tenishev, A. F. Nagy, Three-dimensional study of Mars upper thermosphere-ionosphere and hot oxygen corona: Solar cycle, seasonal variations and evolution over history. *J. Geophys. Res.* **114**, E11006 (2009). doi: [10.1029/2009JE003389](https://doi.org/10.1029/2009JE003389)
- W. B. Hanson, S. Sananati, D. R. Zuccaro, The Martian ionosphere as observed by the Viking retarding potential analyzers. *J. Geophys. Res.* **82**, 4351–4363 (1977). doi: [10.1029/JS082i028p04351](https://doi.org/10.1029/JS082i028p04351)
- P. R. Mahaffy et al., Abundance and isotopic composition of gases in the martian atmosphere from the Curiosity rover. *Science* **341**, 263–266 (2013). pmid: [23869014](https://pubmed.ncbi.nlm.nih.gov/23869014/)
- D. Snowden et al., The thermal structure of Titan's upper atmosphere, I. Temperature profiles from Cassini INMS observations. *Icarus* **226**, 552–582 (2013). doi: [10.1016/j.icarus.2013.06.006](https://doi.org/10.1016/j.icarus.2013.06.006)
- P. R. Mahaffy et al., Structure and composition of the neutral upper atmosphere of Mars from the MAVEN NGIMS investigation. *Geophys. Res. Lett.* **42**, (2015). doi: [10.1002/2015GL065329](https://doi.org/10.1002/2015GL065329)
- F. LeBlanc, J. Y. Chauffray, J. Lilenstein, O. Witasse, J.-L. Bertaux, Martian dayglow as seen by the SPICAM UV spectrograph on Mars Express. *J. Geophys. Res.* **111** (E9), E09S11 (2006). doi: [10.1029/2005JE002664](https://doi.org/10.1029/2005JE002664)
- A. Stiepen et al., Mars thermospheric scale height: CO Cameron and CO_2 dayglow observations from Mars Express. *Icarus* **245**, 295–305 (2015). doi: [10.1016/j.icarus.2014.09.051](https://doi.org/10.1016/j.icarus.2014.09.051)
- A. S. Medvedev, E. Yiğit, P. Hartogh, E. Becker, Influence of gravity waves on the Martian atmosphere: General circulation modeling. *J. Geophys. Res.* **116** (E10), E10004 (2011). doi: [10.1029/2011JE003848](https://doi.org/10.1029/2011JE003848)

20. A. Medvedev, E. Yigit, Thermal effects of internal gravity waves in the Martian upper atmosphere. *Geophys. Res. Lett.* **39**, L05201 (2012). doi: [10.1029/2012GL050852](https://doi.org/10.1029/2012GL050852)
21. The exobase of a given planetary upper atmosphere is traditionally estimated as the altitude at which, for a single constituent atmosphere, the collision mean free path equals the temperature scale height of this constituent. For Mars, atomic O is the dominant species considered, and calculated global averaged exobase heights vary from ~170 km (Equinox, solar minimum conditions) to ~185 km (Equinox, solar maximum conditions) (43). In reality, the exobase is not a fixed altitude that separates collisional (thermosphere) and collisionless (exosphere) regimes. Instead, a full transitional domain must be considered, which extends from the altitude at which a hot O particle produced in this region has a high probability to be thermalized to an altitude at which the collision frequency is very low. Modern hot O exosphere models confirm that this transitional domain extends from ~135 to 300 km altitude (43). The ~200 km altitude is commonly used as an approximation for the traditional exobase altitude.
22. A. F. Nagy *et al.*, The plasma environment of Mars. *Space Sci. Rev.* **111**, 33–114 (2004). doi: [10.1023/B:SPAC.0000032718.47512.92](https://doi.org/10.1023/B:SPAC.0000032718.47512.92)
23. E. Dubinin *et al.*, Plasma morphology at Mars. ASPERA-3 observations. *Space Sci. Rev.* **126**, 209–238 (2006). doi: [10.1007/s11214-006-9039-4](https://doi.org/10.1007/s11214-006-9039-4)
24. M. H. G. Zhang, J. G. Luhmann, A. J. Kliore, J. Kim, A post-Pioneer Venus reassessment of the Martian dayside ionosphere as observed by radio occultation methods. *J. Geophys. Res.* **95** (B9), 14,829–14,839 (1990). doi: [10.1029/JB095iB09p14829](https://doi.org/10.1029/JB095iB09p14829)
25. D. A. Gurnett *et al.*, Large density fluctuations in the Martian ionosphere as observed by the Mars Express radar sounder. *Icarus* **206**, 83–94 (2010). doi: [10.1016/j.icarus.2009.02.019](https://doi.org/10.1016/j.icarus.2009.02.019)
26. P. Withers, A review of observed variability in the dayside ionosphere of Mars. *Adv. Space Res.* **44**, 277–307 (2009). doi: [10.1016/j.asr.2009.04.027](https://doi.org/10.1016/j.asr.2009.04.027)
27. F. Duru *et al.*, Steep, transient density gradients in the Martian ionosphere similar to the ionopause at Venus. *J. Geophys. Res.* **114** (A12), A12310 (2009). doi: [10.1029/2009JA014711](https://doi.org/10.1029/2009JA014711)
28. J. E. P. Connerney *et al.*, The MAVEN magnetic field investigation. *Space. Sci. Rev.* 10.1007/s11214-015-0169-4 (2015).
29. J. S. Halekas *et al.*, The Solar Wind Ion Analyzer for MAVEN. *Space Sci. Rev.* (2013). doi: [10.1007/s11214-013-0029-z](https://doi.org/10.1007/s11214-013-0029-z)
30. R. Ergun *et al.*, Dayside electron temperature and density profiles at Mars: First results from the MAVEN Langmuir Probe and Waves instrument. *Geophys. Res. Lett.* **42**, (2015). doi: [10.1002/2015GL065280](https://doi.org/10.1002/2015GL065280)
31. J. L. Fox, A. Dalgarno, Ionization, luminosity, and heating of the upper atmosphere of Mars. *J. Geophys. Res.* **84** (A12), 7315 (1979). doi: [10.1029/JA084iA12p07315](https://doi.org/10.1029/JA084iA12p07315)
32. A. J. Kopf, D. A. Gurnett, D. M. Morgan, D. L. Kirchner, Transient layers in the topside ionosphere of Mars. *Geophys. Res. Lett.* **35**, L17102 (2008). doi: [10.1029/2008GL034948](https://doi.org/10.1029/2008GL034948)
33. P. Withers *et al.*, A clear view of the multifaceted dayside ionosphere of Mars. *Geophys. Res. Lett.* **39**, L18202 (2012). doi: [10.1029/2012GL053193](https://doi.org/10.1029/2012GL053193)
34. H. Shinagawa, T. E. Cravens, The ionospheric effects of a weak intrinsic magnetic field at Mars. *J. Geophys. Res.* **97** (E1), 1027–1035 (1992). doi: [10.1029/91JE02720](https://doi.org/10.1029/91JE02720)
35. S. Kirkwood, H. Nilsson, Kirkwood and Nilsson, High-latitude sporadic-E and other thin layers – the role of magnetospheric electric fields. *Space Sci. Rev.* **91**, 579–613 (2000). doi: [10.1023/A:1005241931650](https://doi.org/10.1023/A:1005241931650)
36. J. L. Fox, K. E. Yeager, Morphology of the near-terminator Martian ionosphere: A comparison of models and data. *J. Geophys. Res.* **111** (A10), A10309 (2006). doi: [10.1029/2006JA011697](https://doi.org/10.1029/2006JA011697)
37. C. Dong *et al.*, Solar wind interaction with Mars upper atmosphere: Results from the one-way coupling between the multi-fluid MHD model and the MTGCM model. *Geophys. Res. Lett.* **41**, 2708–2715 (2014). doi: [10.1002/2014GL059515](https://doi.org/10.1002/2014GL059515)
38. C. Dong *et al.*, Solar wind interaction with the Martian upper atmosphere: Crustal field orientation, solar cycle, and seasonal variations. *J. Geophys. Res.* **120**, (2015). doi: [10.1002/2015JA020990](https://doi.org/10.1002/2015JA020990)
39. E. Kallio, S. Barabash, Atmospheric effects of precipitating energetic hydrogen atoms on the Martian atmosphere. *J. Geophys. Res.* **106** (A1), 165–177 (2001). doi: [10.1029/2000JA002003](https://doi.org/10.1029/2000JA002003)
40. J. S. Halekas *et al.*, MAVEN observations of solar wind hydrogen deposition in the atmosphere of Mars. *Geophys. Res. Lett.* **42**, (2015). doi: [10.1002/2015GL064693](https://doi.org/10.1002/2015GL064693)
41. J. Luhmann, J. U. Kozyra, Dayside Pickup Oxygen Ion Precipitation at Venus and Mars - Spatial Distributions, Energy Deposition and Consequences. *J. Geophys. Res.* **96** (A4), 5457–5467 (1991). doi: [10.1029/90JA01753](https://doi.org/10.1029/90JA01753)
42. D. Najib, A. Nagy, G. Toth, Y. Ma, Three-dimensional, multi-fluid, high spatial resolution MHD model studies of the solar wind interaction with Mars. *J. Geophys. Res.* (2011). doi: [10.1029/2010JA016272](https://doi.org/10.1029/2010JA016272)
43. Y. Lee, M. Combi, V. Tenishev, S. Bouger, D. Pawlowski, N. Franklin, Impacts of the Martian crustal magnetic fields on the thermosphere, ionosphere, and hot oxygen corona. *Bulletin of the American Astronomical Society*, **46**, abstract 306.01, Div. for Planetary Sciences, 46th Annual Meeting, Tucson, AZ (2014).

ACKNOWLEDGMENTS

The MAVEN Deep Dip 2 data sets reported in the paper are archived on the public version of the MAVEN Science Data Center (SDC) website, at the LASP url (<https://lasp.colorado.edu/maven/sdc/public/>) and on the Planetary Data System (PDS). Datacubes from three-dimensional model simulations reported in this paper are also available on the public MAVEN SDC website at <https://lasp.colorado.edu/maven/sdc/public/pages/models.html>. This work was partially supported by the Centre National d’Études Spatiales for the part based on observations with the SWEA instrument embarked on Maven. Part of this research was also carried out at the Jet Propulsion Laboratory, California Institute of Technology, under a contract with the National Aeronautics and Space Administration (NASA). A. Stiepen was supported by the Belgian American Educational Foundation and the Rotary District 1630. G. DiBraccio was supported by a NASA Postdoctoral Program appointment at NASA Goddard Space Flight Center, administered by Oak Ridge Associated Universities through a contract with NASA. The MAVEN project is supported by NASA through the Mars Exploration Program.

SUPPLEMENTARY MATERIALS

www.sciencemag.org/content/350/6261/aad0459/suppl/DC1
Supplementary Text

17 July 2015; accepted 21 September 2015
10.1126/science.aad0459

This copy is for your personal, non-commercial use only.

If you wish to distribute this article to others, you can order high-quality copies for your colleagues, clients, or customers by [clicking here](#).

Permission to republish or repurpose articles or portions of articles can be obtained by following the guidelines [here](#).

The following resources related to this article are available online at
www.sciencemag.org (this information is current as of November 5, 2015):

Updated information and services, including high-resolution figures, can be found in the online version of this article at:

<http://www.sciencemag.org/content/350/6261/aad0459.full.html>

Supporting Online Material can be found at:

<http://www.sciencemag.org/content/suppl/2015/11/04/350.6261.aad0459.DC1.html>

A list of selected additional articles on the Science Web sites related to this article can be found at:

<http://www.sciencemag.org/content/350/6261/aad0459.full.html#related>

This article cites 37 articles, 2 of which can be accessed free:

<http://www.sciencemag.org/content/350/6261/aad0459.full.html#ref-list-1>

This article has been cited by 1 articles hosted by HighWire Press; see:

<http://www.sciencemag.org/content/350/6261/aad0459.full.html#related-urls>